



The Preexplosion Environments and the Progenitor of SN 2023ixf from the Hobby–Eberly Telescope Dark Energy Experiment (HETDEX)

Chenxu Liu¹ , Xinlei Chen¹ , Xinzhong Er¹ , Gregory R. Zeimann² , József Vinkó^{3,4,5,6} , J. Craig Wheeler³ , Erin Mentuch Cooper^{2,3} , Dustin Davis³ , Daniel J. Farrow^{7,8} , Karl Gebhardt³ , Helong Guo¹ , Gary J. Hill^{2,3} , Lindsay House³ , Wolfram Kollatschny⁹ , Fanchuan Kong¹ , Brajesh Kumar¹ , Xiangkun Liu¹ , Sarah Tuttle¹⁰ , Michael Endl³ , Parker Duke³ , William D. Cochran^{2,11} , Jinghua Zhang¹ , and Xiaowei Liu¹

¹ South-Western Institute for Astronomy Research, Yunnan University, Kunming, Yunnan, 650500, People's Republic of China; cxliu@ynu.edu.cn

² McDonald Observatory, The University of Texas at Austin, 2515 Speedway Boulevard, Austin, TX 78712, USA

³ Department of Astronomy, The University of Texas at Austin, 2515 Speedway Boulevard, Austin, TX 78712, USA

⁴ Konkoly Observatory, CSFK, Konkoly-Thege M. út 15-17, Budapest, 1121, Hungary

⁵ ELTE Eötvös Loránd University, Institute of Physics, Pázmány Péter sétány 1/A, Budapest, 1117 Hungary

⁶ Department of Experimental Physics, University of Szeged, Dóm tér 9, Szeged, 6720, Hungary

⁷ Centre of Excellence for Data Science, Artificial Intelligence and Modelling, University of Hull, Cottingham Road, Hull, HU6 7RX, UK

⁸ E.A. Milne Centre for Astrophysics, University of Hull, Cottingham Road, Hull, HU6 7RX, UK

⁹ Institut für Astrophysik und Geophysik, Universität Göttingen, Friedrich-Hund Platz 1, D-37077 Göttingen, Germany

¹⁰ Department of Astronomy, University of Washington, Seattle, Physics & Astronomy Building, Seattle, WA 98195, USA

¹¹ Center for Planetary Systems Habitability, The University of Texas at Austin, Austin, TX 78712, USA

Received 2023 September 12; revised 2023 November 8; accepted 2023 November 17; published 2023 November 30

Abstract

Supernova (SN) 2023ixf was discovered on 2023 May 19. The host galaxy, M101, was observed by the Hobby–Eberly Telescope Dark Energy Experiment collaboration over the period 2020 April 30–2020 July 10, using the Visible Integral-field Replicable Unit Spectrograph ($3470 \lesssim \lambda \lesssim 5540 \text{ \AA}$) on the 10 m Hobby–Eberly Telescope. The fiber filling factor within $\pm 30''$ of SN 2023ixf is 80% with a spatial resolution of $1''$. The $r < 5''.5$ surroundings are 100% covered. This allows us to analyze the spatially resolved preexplosion local environments of SN 2023ixf with nebular emission lines. The two-dimensional maps of the extinction and the star formation rate (SFR) surface density (Σ_{SFR}) show weak increasing trends in the radial distributions within the $r < 5''.5$ regions, suggesting lower values of extinction and SFR in the vicinity of the progenitor of SN 2023ixf. The median extinction and that of the surface density of SFR within $r < 3''$ are $E(B - V) = 0.06 \pm 0.14$, and $\Sigma_{\text{SFR}} = 10^{-5.44 \pm 0.66} M_{\odot} \text{ yr}^{-1} \text{ arcsec}^{-2}$. There is no significant change in extinction before and after the explosion. The gas metallicity does not change significantly with the separation from SN 2023ixf. The metal-rich branch of the R_{23} calculations indicates that the gas metallicity around SN 2023ixf is similar to the solar metallicity ($\sim Z_{\odot}$). The archival deep images from the Canada–France–Hawaii Telescope Legacy Survey (CFHTLS) show a clear detection of the progenitor of SN 2023ixf in the z band at 22.778 ± 0.063 mag, but nondetections in the remaining four bands of CFHTLS (u, g, r, i). The results suggest a massive progenitor of $\approx 22 M_{\odot}$.

Unified Astronomy Thesaurus concepts: [Supernovae \(1668\)](#)

1. Introduction

The life of a massive star ends with a dramatic and energetic explosion known as a core-collapse supernova (CCSN; Branch & Wheeler 2017). These impressive events present a unique opportunity to delve into the physics of massive star evolution and the creation of heavy elements through nucleosynthesis. It has been discovered that the progenitor stars of CCSNe experienced eruptive mass loss in the years prior to the core collapse (e.g., Smith 2014). Pre-SN outbursts are often observed especially in Type II_n that display narrow emission lines for extended times after the explosion (e.g., Ofek et al. 2014) as a consequence of the shock interaction between the slow-moving circumstellar medium (CSM) and the ejected material of the explosion (Smith 2014). However, the underlying physical mechanism that triggers those outbursts and the mass loss rates involved remain elusive (e.g., Beasor et al. 2020; Gofman et al. 2020; Humphreys et al. 2020;

Hosseinzadeh et al. 2022; Ou et al. 2023). Direct identification of progenitors and the environments of stars via preexplosion imaging becomes crucial in understanding these unsolved questions. Nonetheless, resolving individual stars in external galaxies at large distances is challenging, making the detection and study of SN events in nearby galaxies particularly important.

SN 2023ixf was reported on 2023 May 19.727 UT in M101 (NGC 5457; Itagaki 2023) and was classified as a Type II SN (Perley et al. 2023). Being the SN event of the smallest distance in the past decade, intensive archival observations are available to identify the progenitor and to constrain the preexplosion environment (e.g., Dong et al. 2023; Hiramatsu et al. 2023; Jacobson-Galan et al. 2023; Jencson et al. 2023; Kilpatrick et al. 2023; Neustadt et al. 2023; Pledger & Shara 2023; Soker 2023; Soraisam et al. 2023; Van Dyk et al. 2023).

M101 is an Scd-type galaxy with active star formation (Lin et al. 2013). Several SNe events have been identified in the past century, e.g., the extensively studied SN 2011fe. Detailed comparison of the environments before and after the SN explosion may provide a direct constraint to the nature of SN feedback in the study of galaxy formation. Here we report the



Original content from this work may be used under the terms of the [Creative Commons Attribution 4.0 licence](#). Any further distribution of this work must maintain attribution to the author(s) and the title of the work, journal citation and DOI.

detection of the candidate progenitor star in the archival data from the Canada–France–Hawaii Telescope Legacy Survey (CFHTLS). We analyze the preexplosion environments of the progenitor using integral field spectroscopic observation from the Hobby–Eberly Telescope Dark Energy Experiment (HETDEX). In this work, we use the distance estimate of the host galaxy 6.85 ± 0.15 Mpc reported by Riess et al. (2022) and the redshift estimate of $z = 0.000804$ (Perley et al. 2023). The coordinates of SN 2023ixf are (R.A. = 210.910674637, Decl. = +54.3116510708, J2000).¹²

2. Data

2.1. HETDEX

HETDEX (Gebhardt et al. 2021) is an untargeted spectroscopic survey aimed at constraining the nature of dark energy by mapping out the three-dimensional distribution of Ly α emitting galaxies between the redshifts $1.9 < z < 3.5$. This survey is being carried out on the upgraded 10 m Hobby–Eberly Telescope (HET) with a segmented spherical primary mirror (Ramsey et al. 1994; Hill et al. 2021) and a 22' aberration-corrected field of view. The upgraded HET includes a new instrument called the Visible Integral-field Replicable Unit Spectrograph (VIRUS), which is a massively replicated, fiber-fed integral field spectrograph (Hill et al. 2021) designed specifically to identify emission-line objects. VIRUS consists of 78 Integral Field Units (IFUs), each containing 448 1''5-diameter fibers packed into a 51'' \times 51'' array. Each IFU feeds two low-resolution ($R \sim 800$) spectrographs, together covering the wavelength range $3470 \lesssim \lambda \lesssim 5540$ Å. At the project's nominal depth, the spectra reach a 5σ completeness of 3.5×10^{-17} erg cm $^{-2}$ s $^{-1}$ at [O III] $\lambda 5007$.

A typical HETDEX observation uses a three-point dither pattern to fill in the gaps between fibers, with each dithered exposure being 6 minutes in length. The IFUs themselves are distributed in a grid, with each IFU separated from its nearest neighbor by 50'' (except in the very center of the array, where other HET instruments are located). The result is that each HETDEX observation has a fiber-fill factor of 1 in 4.5. M101 lies within the footprint of the HETDEX survey, but to facilitate studies of the galaxy, additional pointings were defined to give a near-complete fill factor of 1. The data of the full M101 observations were collected over the period 2020 April 30–2020 July 10, during a time when ~ 70 of the planned 78 VIRUS IFUs were operational.

In total, there are 21 HETDEX observations covering the M101 field. Unlike the main HETDEX survey design, the footprint was chosen to provide as complete sky coverage as possible with tiling designed to fill in the gaps between the IFU array of the VIRUS spectrograph. We generate a datacube mosaic from this set of observations using a different reduction method than that described in Gebhardt et al. (2021). The HETDEX observations of M101 were processed by Remedy.¹³ Here we briefly summarize the data reduction and calibration of the M101 observations, but further details are found in G. R. Zeimann et al. (2023, in preparation). Astrometry is determined by matching wavelength collapsed images produced from the VIRUS spectra with stars within the Pan-STARRS (Chambers et al. 2016) Data Release 2 catalog.

The rms of the star's positions about the solution is $\lesssim 0''.25$ and the rms of the solution is typically less than $\lesssim 0''.05$.

In typical HETDEX observations, as described in Gebhardt et al. (2021), flux calibration is determined using field stars of the Sloan Digital Sky Survey (SDSS; York et al. 2000). However, in the case of M101, where there are no SDSS fields available, we simply adopt an average throughput curve from all HETDEX observations, adjusted for the conditions of that observation. We normalize our response curves to the monochromatic fluxes obtained from the narrowband [O III] $\lambda 5007$ images of K. Herrmann et al. (2023, in preparation). To do this, we apply the narrowband filter's transmission curve¹⁴ to VIRUS spectra to create a [O III] $\lambda 5007$ synthetic image. We then smooth both the synthetic image and Mosaic image to account for differential seeing, and use the biweight of the ratio of these two images to normalize each observation's response curve.

We construct a single data cube for all HETDEX observations in the area of M101, centered at R.A. = 210°800 and Decl. = 54°333 with spectral pixels of $1'' \times 1'' \times 2$ Å. To go from the nonuniform sky positions of the fibers to the uniform grid of the data cube, we placed each fiber's flux into the nearest pixel at every wavelength. If multiple fibers from multiple observations contributed to the same pixel, we calculated the median value. All pixels without a flux contribution from a fiber were masked. We then performed a Gaussian convolution using a seeing of 1''.8 to reconstruct the image at each wavelength. The final data cube is $1201 \times 1201 \times 1036$ pixels.

2.2. CFHTLS

The Canada–France–Hawaii Telescope Legacy Survey (CFHTLS) is a deep subarcsecond ($0''.8$) wide-field (157 deg 2 total) optical survey with u, g, r, i, z bands. The seventh and final release of CFHTLS (CFHTLS-T0007; Cuillandre et al. 2012) is produced by TERAPIX based on a data set collected with MagCam with 36 charge-coupled devices (CCDs) on the CFHT. M101 lies within the footprint of the CFHTLS-T0007. It was observed in the i and z bands on 2005 May 11, and 2006 June 7, respectively. These observations included six consecutive images with 615 s exposures in the i band and 600 s exposures in the z band.

3. Preexplosion Environments

Figure 1 shows the HETDEX image of SN 2023ixf created from the integrated flux within [3550, 5450] Å. The bluest wavelengths and the reddest wavelengths are not used to avoid potential edge effects from CCDs. The white gaps are the pixels with no fiber coverage. This $60'' \times 60''$ cutout has a fiber coverage of 80%. The red circle marks the $r < 5''.5$ region, within which the fiber coverage is 100%. This region does not include the fibers on the edges of IFUs. The flux of edge fibers can be potentially overestimated due to large aperture corrections. Therefore, the $r < 5''.5$ region is selected for the study of the preexplosion environments.

Figure 2 shows the spectrum of the HETDEX pixel closest to SN 2023ixf. The center of this pixel is $0''.54$ away from SN 2023ixf. As shown by the six panels in the bottom two rows, the nebular emissions of [O II] $\lambda 3727$, H γ , H β , [O III] $\lambda 4959$, and [O III] $\lambda 5007$ are significantly detected within our

¹² <https://www.wis-tns.org/object/2023ixf>

¹³ <https://github.com/grzeimann/Remedy>

¹⁴ <https://www.noao.edu/kpno/mosaic/filters/k1014.html>

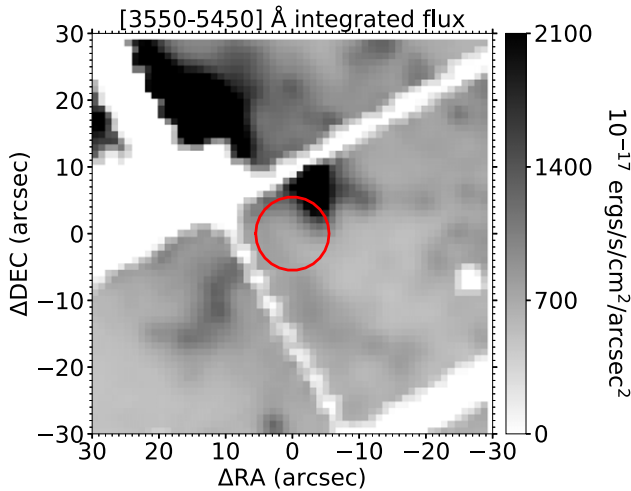


Figure 1. The $\pm 30''$ HETDEX image cutout centered on SN 2023ixf taken in the year of 2020. The image is created from the integrated flux within the wavelength range of [3550, 5450] Å. The pixel size is $1'' \times 1''$. The red circle shows the region of $r < 5''.5$, which is selected for the study of the local environments.

wavelength range. The $H\delta$ emission can be marginally recovered after stellar subtraction using the templates of Bruzual & Charlot (2003, hereafter BC03). These nebular lines allow the estimates of extinction (Section 3.1), gas metallicity (Section 3.2), and star formation rates (SFRs; Section 3.3). It is worth noting that no significant variations of the line widths or redshifts/blueshifts of the emission lines are detected as a function of the distance to the SN center with our 2 \AA resolution. However, a velocity below our resolution could not be ruled out.

3.1. Extinction

The gas extinction $E(B - V)_{\text{gas}}$ can be derived from the Balmer decrement. In this paper, due to the limitation of the wavelength coverage of HETDEX, we use the $H\gamma/H\beta$ ratio instead of the more commonly used $H\beta/H\alpha$ ratio to calculate the gas extinction. We assume a Galactic extinction curve ($R_V = A_V/E(B - V) = 3.1$) (Cardelli et al. 1989) and an intrinsic $H\gamma/H\beta$ ratio of 0.47 ($T = 15,000 \text{ K}$, case B recombination; Storey & Hummer 1995). The reddening suffered by the stellar continuum from the interstellar medium (ISM) $E(B - V)_{\text{ISM}}$ can then be roughly estimated as 0.44 times the reddening suffered by the ionized gas $E(B - V)_{\text{gas}}$ (Calzetti 2001).

Figure 3 shows the extinction map in the upper left panel and its radial variations in the upper right panel. Only pixels with both the $H\gamma$ and $H\beta$ emission lines strong enough, equivalent widths (EWs) greater than 3 \AA , are calculated with their extinctions and shown. There is a weak increment of the extinction as a function of the separations from SN 2023ixf. The median values of $E(B - V)_{\text{ISM}}$ of all pixels within $r < 1''$, $3''$, and $4''.5$ are $0.03 \pm 0.06 \text{ mag}$, $0.06 \pm 0.14 \text{ mag}$, and $0.13 \pm 0.18 \text{ mag}$, respectively. For M101 exhibiting very high SFRs, the mean Galactic extinction curve may not be suitable, and the value of R_V can be much larger (e.g., ~ 4.05 ; Calzetti 1997). This will give slightly higher measurements of the extinction ($\Delta E(B - V)_{\text{ISM}} \lesssim 0.01 \text{ mag}$), but the weak increasing trend will remain.

Two high-resolution spectra on SN2033ixf were taken with the cross-dispersed echelle spectrograph (TS2; resolving power

$R = 60,000$) on the 2.7 m Harlan J. Smith Telescope at McDonald Observatory 2023 May 22.72 and 2023 June 14.66 UT. Resolved components of the narrow NaD doublet at the redshift of M101 ($z = 0.000804$) were clearly detected. EWs of the D1 and D2 components (187.3 and 126.3 mÅ, respectively) correspond to $E(B - V) = 0.033 \pm 0.03 \text{ mag}$ using the formulae of Poznanski et al. (2012). This is in perfect agreement with the results of Jacobson-Galan et al. (2023), Lundquist et al. (2023), Smith et al. (2023), and Hiramatsu et al. (2023), and it is not significantly different from our preexplosion measurement of $E(B - V) = 0.03 \pm 0.06$ in the regions of $r < 1''$. Niu et al. 2023 measure the preexplosion extinction of the environment within $r < 4''.5$ as $E(B - V) = 0.15 \text{ mag}$ using the resolved stars in the Hubble Space Telescope (HST) images. This is consistent with our median $E(B - V) = 0.13 \pm 0.18 \text{ mag}$ in the regions of $r < 4''.5$.

3.2. Gas Metallicity

We use the R_{23} strong-line method to estimate the gas metallicity (Z), where R_{23} is a line ratio defined as $\frac{[\text{O III}]\lambda 3727 + [\text{O III}]\lambda 4959, 5007]}{H\beta}$ (e.g., Tremonti et al. 2004). Line fluxes are dereddened using the gas extinction derived in Section 3.1 and the extinction law of Cardelli et al. (1989). For a given R_{23} , there are two associated metallicity values, one is in the metal-poor branch, and the other is in the metal-rich branch (e.g., Kobulnicky et al. 1999). SN 2023ixf is $\sim 4.5 \text{ kpc}$ away from the center of M101, which is within the break radius in the abundance gradient at 15.4 kpc (Garner et al. 2022). This suggests that the surroundings of SN 2023ixf would probably favor the metal-rich branch. However, the possibility of the metal-poor branch can not be fully ruled out.

Figure 3 shows the metallicity map derived from the metal-rich branch in the middle left panel. In the middle right panel, both the radial variations of the metallicity from the metal-rich branch (solid upper triangles) and those of the metallicity from the metal-poor branch (open lower triangles) are shown. We only calculate the metallicity for pixels that satisfy the following criteria: $EW_{[\text{O III}]\lambda 3727} > 3 \text{ \AA}$, $EW_{[\text{O III}]\lambda 5007} > 3 \text{ \AA}$, and $EW_{H\beta} > 3 \text{ \AA}$. Assuming all pixels around SN 2023ixf following the metal-rich branch, the median O abundances of all pixels within $r < 1''$, $3''$, and $4''.5$ are $12 + \log(\text{O}/\text{H})_{\text{upper}} = 8.66 \pm 0.05$, 8.65 ± 0.11 , and 8.61 ± 0.11 , respectively. Considering the scattering, the gas metallicity does not change significantly with their separations from SN 2023ixf. Assuming a solar O abundance of $12 + \log(\text{O}/\text{H})_{\odot} = 8.69$ and a solar metallicity of $Z_{\odot} = 0.013$ (Asplund et al. 2021), the metal-rich branch gives a metallicity of $Z \sim 0.013 \pm 0.002$ ($\sim Z_{\odot}$), and the metal-poor branch gives $Z \sim 0.003 \pm 0.001$ ($12 + \log(\text{O}/\text{H})_{\text{lower}} = 8.04 \pm 0.09 \text{ dex}$, $\sim 0.25Z_{\odot}$). We note that considering a more recent solar O abundance estimation of $12 + \log(\text{O}/\text{H})_{\odot} = 8.77$ and a solar metallicity of $Z_{\odot} = 0.0225$ from Magg et al. (2022), the metal-rich branch would give a metallicity of $Z \sim 0.018 \pm 0.002$, and the metal-poor branch gives $Z \sim 0.004 \pm 0.001$.

Pledger & Shara (2023) reported the preexplosion O abundances of two near the SN site H II regions published in Kennicutt & Garnett (1996; region 1098 and 1086 in their Figure 2(b)) as $12 + \log(\text{O}/\text{H})_{\text{upper}} = 8.63$ and 8.59 , which are close to our preexplosion on-site results observed in the year of 2020. Van Dyk et al. (2023) analyzed the after-explosion on-site O abundances to be $8.43 \lesssim 12 + \log(\text{O}/\text{H}) \lesssim 8.86$ from Gemini Spectroscopy on 2023 June 3. The metallicity does not change significantly after the SN 2023ixf event.

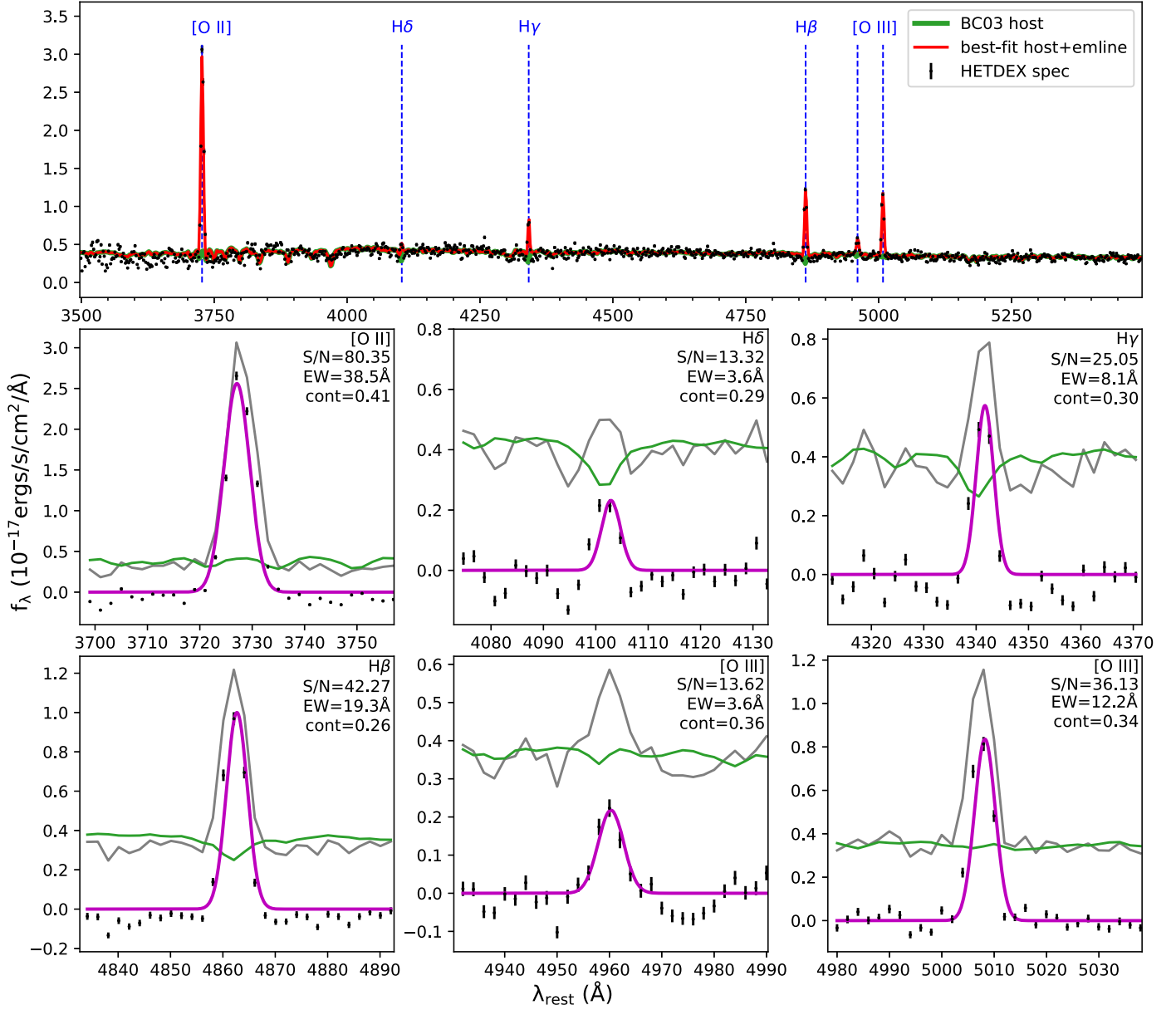


Figure 2. The spectrum of the HETDEX pixel closest to SN 2023ixf. The top panel shows the spectrum in the full HETDEX wavelength range with the black data points. The red line is our best-fit spectrum consisting of the best-fit stellar continuum using BC03 templates and the best-fit emission lines. The blue dashed lines mark the emission lines. The six panels in the second and third rows show the subregions of the six emission lines: [O II] $\lambda 3727$, H δ , H γ , H β , [O III] $\lambda 4959$, and [O III] $\lambda 5007$. The green lines are the best-fit stellar continuum in all seven panels. The gray curves in all panels of the bottom two rows are the HETDEX spectrum in each wavelength range. The black data points in the bottom two rows show the continuum-subtracted spectra. The magenta lines are the best-fit emission line profiles.

3.3. Surface Density of Star Formation Rates

The commonly used emission-line indicator of the SFR, the H α emission, is out of the wavelength coverage of HETDEX. SFR is therefore estimated using the correlation between the luminosity of [O II] $\lambda 3727$ and SFR (Equation (4) in Kewley et al. 2004). For our case, the calculated SFR of each pixel ($1'' \times 1''$) is the surface density of SFR (Σ_{SFR}) in units of $M_{\odot} \text{ yr}^{-1} \text{ arcsec}^{-2}$.

Figure 3 shows the Σ_{SFR} map in the bottom left panel and its radial variations in the bottom right panel. Again, only pixels with $\text{EW}_{[\text{O II}]\lambda 3727} > 3 \text{ \AA}$ are calculated along with their SFRs. There is an increasing trend of the surface density of SFR as a function of the separations from SN 2023ixf. The median $\log \Sigma_{\text{SFR}}$ of all pixels within $r < 1''$, $3''$, and $4''.5$ are -5.59 ± 0.28 , -5.44 ± 0.66 , and -5.04 ± 0.84 , respectively.

4. Mass of the Progenitor

We reprocessed the images of the progenitor from CFHTLS to obtain the magnitudes of the progenitor in the single-exposure images and in the stacked image. Before stacking the images using swarp,¹⁵ we remove cosmic rays using the python package ccdproc.¹⁶ We then recalibrate the astrometry using scamp,¹⁷ with reference stars from Gaia Data Release 3. SExtractor¹⁸ and PSFEx¹⁹ are used to do the photometry of the progenitor. The photometric zero-point is taken directly from

¹⁵ <https://www.astromatic.net/software/swarp/>

¹⁶ <https://github.com/astropy/ccdproc>

¹⁷ <https://www.astromatic.net/software/scamp/>

¹⁸ <https://www.astromatic.net/software/sextractor/>

¹⁹ <https://www.astromatic.net/software/psfex/>

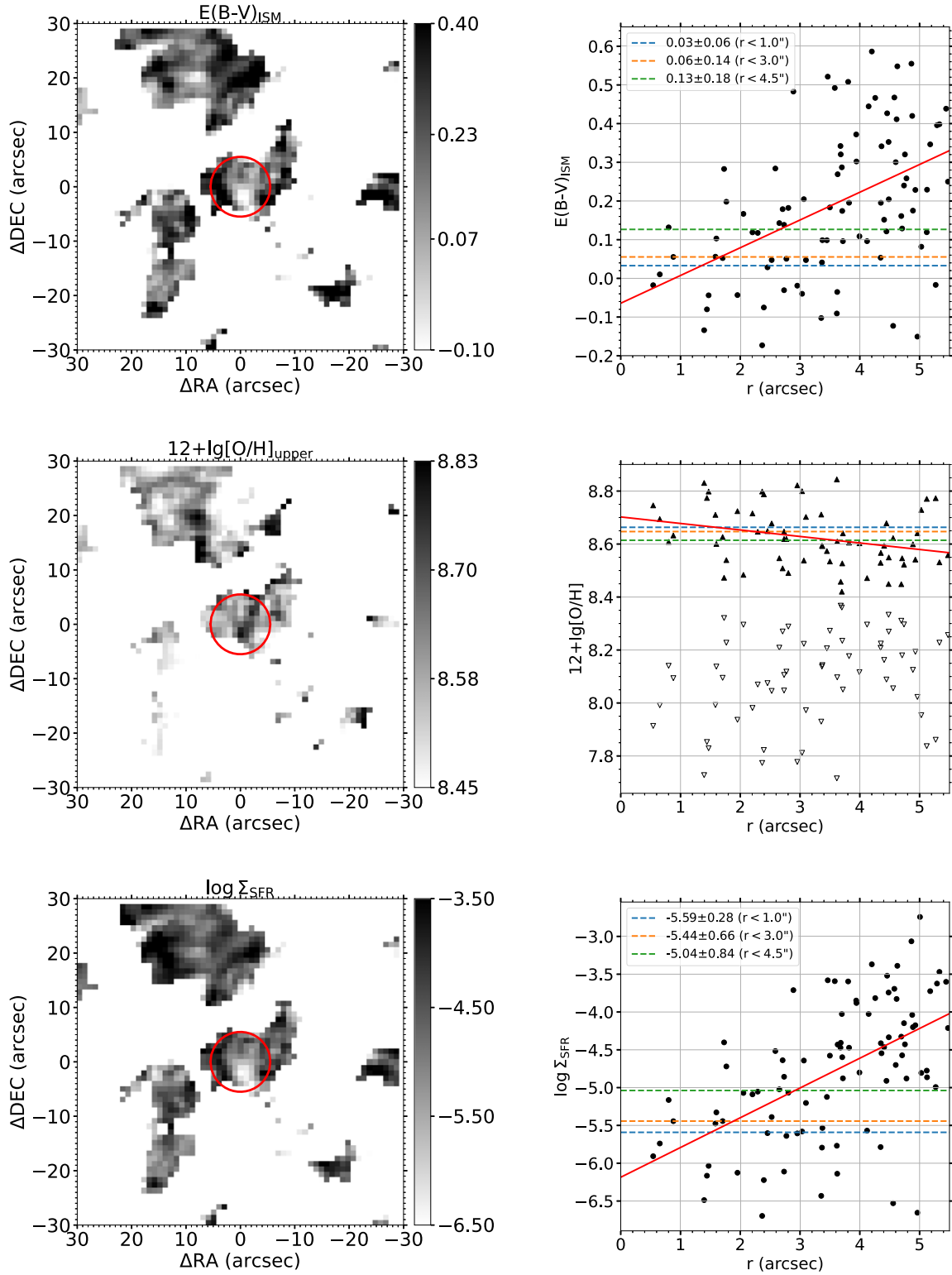


Figure 3. The two-dimensional maps of the diffuse ISM extinction ($E(B - V)_{\text{ISM}}$, top left panel), O abundance derived from the metal-rich branch of the R_{23} method (middle left panel), and the surface density of the star formation rate ($\log \Sigma_{\text{SFR}}$, bottom left panel) centered on SN 2023ixf. Pixels with fiber coverage but not shown are because their nebular emission lines are not strong enough for reliable measurements of the extinction, O abundance, and the star formation rates, see contexts for details. Their variations as a function of the separations from SN 2023ixf are shown in the right panels. Data points in the right panels are associated with the individual pixels with measurements within the red circles in the left panels. The blue, orange, and green dashed lines in the right panels mark the median values of $E(B - V)_{\text{ISM}}$, $12 + \log(\text{O}/\text{H})_{\text{upper}}$, and $\log \Sigma_{\text{SFR}}$ of pixels within $r < 1''$, $3''$, and $4.5''$, respectively. The median values are also labeled in the upper left corners. The red solid lines in the right panels are simple linear fits to all pixels within $r < 5.5''$ (the red circles in the left panels) given to guide the eye to radial trends. In the middle right panel, both the O abundances derived from the metal-rich branch of the R_{23} method (the solid upper triangles) and those derived from the metal-poor branch (open lower triangles) are shown.

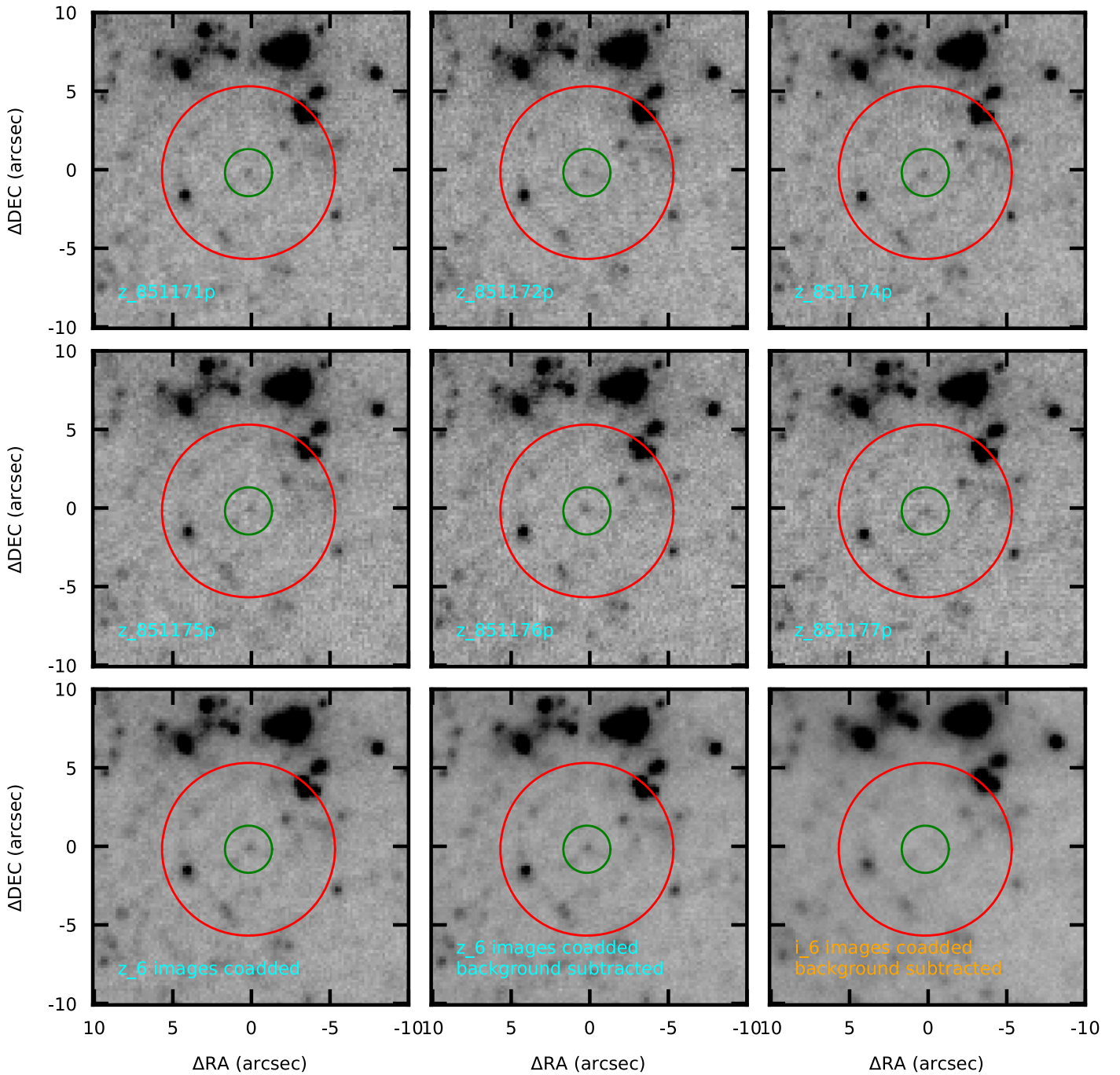


Figure 4. The CFHTLS image cutouts centered on SN 2023ixf. The six panels in the top two rows show the six individual z -band images. The bottom panels show the z -band coadded, the z -band background subtracted coadded, and the i -band background subtracted coadded images from left to right. The z -band observations were taken on 2006 June 7. The i -band observations were taken on 2005 May 11. The green and red circles mark the $r < 1''$ and $r < 5''$ regions of SN 2023ixf, respectively.

the header of the archival fits files. We validate this value using the SDSS survey and the Pan-STARRS survey. z_0 recorded in the header of each individual z -band image is 24.754 mag. We cross match each individual image with the SDSS survey and the Pan-STARRS survey. The zero-point magnitude is then calculated using the common stars recorded in the SDSS survey and the Pan-STARRS survey separately. Take the z -band single exposure 851171p as an example: the derived zero-point from SDSS is $z_0 = 24.761 \pm 0.172$ mag and that derived from Pan-STARRS is $z_0 = 24.753 \pm 0.176$ mag. Both surveys confirm the photometric zero-point $z_0 = 24.754$ mag

recorded in the header. The progenitor is significantly detected in the z band at 22.778 ± 0.063 mag in the stacked images (the bottom left panel and the bottom middle panel of Figure 4). All six individual z -band images show clear detections at the position of SN 2023ixf (top two rows of Figure 4). It is worth noting that the progenitor is also significantly detected in the z -band observation of the Dark Energy Camera Legacy Survey (DECaLS)²⁰ at 23.30 ± 1.58 mag, which confirms our measurements from CFHTLS images. The progenitor is not

²⁰ <https://www.legacysurvey.org/decamls/>

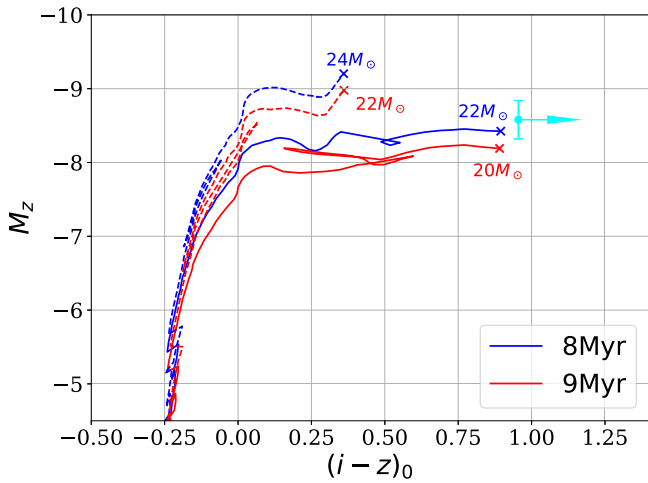


Figure 5. Color–magnitude diagram plotting 8 and 9 Myr PARSEC stellar evolutionary isochrones along with our progenitor candidate. The cyan point is the color–magnitude position measured from CFHTLS images. The solid lines present the isochrones of solar metallicity Z_{\odot} (the gas metallicity derived from the metal-rich branch using the R_{23} method). The dashed lines present those of $0.25Z_{\odot}$ (the gas metallicity derived from the metal-poor branch using the R_{23} method).

detected in the u , g , r , and i bands. The i -band detection limit is 24.57 mag (5σ).

Three sources of extinction have been taken into account: the Milky Way ($E(B - V)_{\text{MW}} = 0.008$ mag; Schlegel et al. 1998; Schlafly & Finkbeiner 2011), the ISM of the host galaxy ($E(B - V)_{\text{ISM}} \sim 0.03$ mag; this work), and the circumstellar medium (CSM) of the progenitor. Here we assume $R_V = 3.1$ for all three sources of extinction. We note that R_V can be slightly higher for ISM in the star-forming regions, which will lead to a slightly brighter and redder measurement. Considering the low $E(B - V)_{\text{ISM}} \sim 0.03$ mag, this would not affect the color and magnitude measurements significantly. Niu et al. (2023) fit the spectral energy distribution (SED) with the C-rich dust models and obtain $E(B - V)_{\text{CSM}} = 1.64 \pm 0.2$ mag. We also note that the C-rich dust model-derived extinction should be applied with caution, as detailed in Section 9.2 of Van Dyk et al. (2023). For the CFHTLS i and z bands, $R_i = 1.799$ and $R_z = 1.299$ are adopted (Zhang & Yuan 2023). These together give $A_i \sim 3.02$ mag and $A_z \sim 2.18$ mag. The distance modulus of the host galaxy is 29.18 (Riess et al. 2022), which gives the absolute magnitudes of the progenitor as $M_i \gtrsim -7.63$ mag (5σ detection limit), $M_z = -8.58$ mag, and a color limit of $M_i - M_z \gtrsim 0.95$.

We use the PARSEC²¹ stellar evolutionary isochrones (Bressan et al. 2012) to estimate the mass of the progenitor (Figure 5). The isochrones that match the CFHTLS color and magnitude best have an age of ~ 8 –9 Myr, an initial mass between ~ 20 and $22 M_{\odot}$, and a solar metallicity $\sim Z_{\odot}$. This metallicity of the progenitor is close to the preexplosion gas metallicity derived from the metal-rich branch in Section 3.2. We also present the evolution of stars with $0.25 Z_{\odot}$ (the preexplosion gas metallicity derived from the metal-poor branch in Section 3.2) by the dashed lines for comparison reasons, although it does not match our color measurement. We note that models with different input evolutionary tracks may result in different initial mass estimates. The widely used

PARSEC isochrones do not fit our $(i - z)$ color limit very well. The solar metallicity isochrones stop at $(i - z)_0 \sim 0.9$, while our color limit of $(i - z) \gtrsim 0.95$ is beyond that. The BPASS (Eldridge et al. 2017) single-star models indicate a lower initial mass range of ~ 15 – $17 M_{\odot}$. We also note that our initial mass estimate is close to the maximum possible mass for SN IIP progenitors $\sim 20 M_{\odot}$ (Davies & Beasor 2020). The z -band magnitude combined with an $(i - z)$ color limit may not constrain the evolution track the best. Jencson et al. (2023) fit the HST photometry and they also concluded with a massive initial mass of $17 \pm 4 M_{\odot}$ for SN 2023ixf. Van Dyk et al. (2023) analyzed the multiband data of SN 2023ixf from HST, Spitzer, Herschel, and Wide-Field IR Survey Explorer (WISE), and their SED fitting indicates a less massive initial mass of ~ 12 – $15 M_{\odot}$.

5. Summary and Discussions

In this paper, we study the preexplosion environments of SN 2023ixf with the HETDEX IFU observations taken in 2020. There are no significant variations of the line widths or redshifts/blueshifts of the emission lines detected as a function of the distance to the SN center with our 2 \AA , or 133 km s^{-1} in velocity space, resolution. We find that SN 2023ixf exploded in a region having low extinction and low SFR locally. This low SFR, however, might be somewhat different from that of the progenitor’s birthplace if the progenitor were a runaway star, like, e.g., Betelgeuse, which has a low velocity of $\sim 30 \text{ km s}^{-1}$ through ISM. Our preexplosion measurement of $E(B - V) = 0.03 \pm 0.06$ mag in the regions of $r < 1''$ based on $H\gamma/H\beta$ line ratio is not significantly different from our after-explosion measurement of $E(B - V) = 0.033 \pm 0.03$ mag from the resolved NaD doublet. The gas metallicity does not vary significantly with their separations from SN 2023ixf. The metal-rich branch of the R_{23} method gives a near solar gas metallicity $\sim Z_{\odot}$ ($12 + \log(\text{O}/\text{H}) = 8.66 \pm 0.05$ dex), and the metal-poor branch gives a gas metallicity of $\sim 0.25 Z_{\odot}$ ($12 + \log(\text{O}/\text{H}) = 8.04 \pm 0.09$ dex). If there are future follow-up observations, especially spatially resolved spectroscopic ones, we will learn more about the SN 2023ixf feedback to the host galaxy by comparing it with our preexplosion measurements of the properties of the surrounding ISM.

We measure the magnitudes of the progenitor of SN 2023ixf in the CFHTLS stack images observed prior to the year 2010. The progenitor is significantly detected in the z -band images at 22.778 ± 0.063 mag, but not detected in the u , g , r , and i bands. A comparatively massive progenitor with an initial mass $\sim 22 M_{\odot}$ and a solar metallicity $\sim Z_{\odot}$ is suggested by comparing the extinction-corrected magnitudes with isochrones. If the local gas environments of SN 2023ixf do follow the metal-rich branch of the R_{23} method, this suggests that the metallicity of the progenitor is comparable with that of the surrounding gas.

Acknowledgments

The authors thank Xiaoting Fu, Wenyu Xin, and Qinghui Sun for valuable suggestions on stellar evolution.

C.X.L., X.L.C., H.L.G., F.C.K., X.K.L., J.H.Z., and X.W.L. acknowledge support from the ‘‘Science & Technology Champion Project’’ (202005AB160002) and from two ‘‘Team Projects’’ - the ‘‘Innovation Team’’ (202105AE160021) and the ‘‘Top Team’’ (202305AT350002), all funded by the ‘‘Yunnan Revitalization Talent Support Program.’’

²¹ <http://stev.oapd.inaf.it/cgi-bin/cmd>

HETDEX is led by the University of Texas at Austin McDonald Observatory and Department of Astronomy with participation from the Ludwig-Maximilians-Universität München, Max-Planck-Institut für Extraterrestrische Physik (MPE), Leibniz-Institut für Astrophysik Potsdam (AIP), Texas A&M University, The Pennsylvania State University, Institut für Astrophysik Göttingen, The University of Oxford, Max-Planck-Institut für Astrophysik (MPA), The University of Tokyo, and Missouri University of Science and Technology. In addition to Institutional support, HETDEX is funded by the National Science Foundation (grant AST-0926815), the State of Texas, the US Air Force (AFRL FA9451-04-2-0355), and generous support from private individuals and foundations.


The Hobby–Eberly Telescope (HET) is a joint project of the University of Texas at Austin, the Pennsylvania State University, Ludwig-Maximilians-Universität München, and Georg-August-Universität Göttingen. The HET is named in honor of its principal benefactors, William P. Hobby and Robert E. Eberly.

VIRUS is a joint project of the University of Texas at Austin, Leibniz-Institut für Astrophysik Potsdam (AIP), Texas A&M University (TAMU), Max-Planck-Institut für Extraterrestrische Physik (MPE), Ludwig-Maximilians-Universität Muenchen, Pennsylvania State University, Institut für Astrophysik Göttingen, University of Oxford, and the Max-Planck-Institut für Astrophysik (MPA). In addition to Institutional support, VIRUS was partially funded by the National Science Foundation, the State of Texas, and generous support from private individuals and foundations.

The authors acknowledge the Texas Advanced Computing Center (TACC) at The University of Texas at Austin for providing high performance computing, visualization, and storage resources that have contributed to the research results reported within this paper. URL:<http://www.tacc.utexas.edu>

The research of J.C.W. and J.V. is supported by NSF AST-1813825. J.V. is also supported by OTKA grant K-142534 of the National Research, Development and Innovation Office, Hungary.

ORCID iDs

Chenxu Liu  <https://orcid.org/0000-0001-5561-2010>
 Xinlei Chen  <https://orcid.org/0009-0000-4068-1320>
 Xinzhong Er  <https://orcid.org/0000-0002-8700-3671>
 Gregory R. Zeimann  <https://orcid.org/0000-0003-2307-0629>
 József Vinkó  <https://orcid.org/0000-0001-8764-7832>
 J. Craig Wheeler  <https://orcid.org/0000-0003-1349-6538>
 Erin Mentuch Cooper  <https://orcid.org/0000-0002-2307-0146>
 Dustin Davis  <https://orcid.org/0000-0002-8925-9769>
 Daniel J. Farrow  <https://orcid.org/0000-0003-2575-0652>
 Karl Gebhardt  <https://orcid.org/0000-0002-8433-8185>
 Helong Guo  <https://orcid.org/0000-0001-5737-6445>
 Gary J. Hill  <https://orcid.org/0000-0001-6717-7685>
 Lindsay House  <https://orcid.org/0000-0002-1496-6514>
 Wolfram Kollatschny  <https://orcid.org/0000-0002-0417-1494>

Fanchuan Kong  <https://orcid.org/0009-0009-9343-090X>
 Brajesh Kumar  <https://orcid.org/0000-0001-7225-2475>
 Xiangkun Liu  <https://orcid.org/0000-0003-0394-1298>
 Sarah Tuttle  <https://orcid.org/0000-0002-7327-565X>
 Michael Endl  <https://orcid.org/0000-0002-7714-6310>
 William D. Cochran  <https://orcid.org/0000-0001-9662-3496>
 Jinghua Zhang  <https://orcid.org/0000-0002-2510-6931>

References

- Asplund, M., Amarsi, A. M., & Grevesse, N. 2021, *A&A*, 653, A141
 Beasar, E. R., Davies, B., Smith, N., et al. 2020, *MNRAS*, 492, 5994
 Branch, D., & Wheeler, J. C. 2017, *Supernova Explosions* (Berlin: Springer)
 Bressan, A., Marigo, P., Girardi, L., et al. 2012, *MNRAS*, 427, 127
 Bruzual, G., & Charlot, S. 2003, *MNRAS*, 344, 1000
 Calzetti, D. 1997, *AJ*, 113, 162
 Calzetti, D. 2001, *PASP*, 113, 1449
 Cardelli, J. A., Clayton, G. C., & Mathis, J. S. 1989, *ApJ*, 345, 245
 Chambers, K. C., Magnier, E. A., Metcalfe, N., et al. 2016, arXiv:1612.05560
 Cuillandre, J.-C. J., Withington, K., Hudelot, P., et al. 2012, *Proc. SPIE*, 8448, 84480M
 Davies, B., & Beasar, E. R. 2020, *MNRAS*, 493, 468
 Dong, Y., Sand, D. J., Valenti, S., et al. 2023, *ApJ*, 957, 28
 Eldridge, J. J., Stanway, E. R., Xiao, L., et al. 2017, *PASA*, 34, e058
 Garner, R., Mihos, J. C., Harding, P., Watkins, A. E., & McGaugh, S. S. 2022, *ApJ*, 941, 182
 Gebhardt, K., Mentuch Cooper, E., Ciardullo, R., et al. 2021, *ApJ*, 923, 217
 Gofman, R. A., Gluck, N., & Soker, N. 2020, *MNRAS*, 494, 5230
 Hill, G. J., Lee, H., MacQueen, P. J., et al. 2021, *AJ*, 162, 298
 Hiramatsu, D., Tsuna, D., Berger, E., et al. 2023, *ApJL*, 955, L8
 Hosseinzadeh, G., Kilpatrick, C. D., Dong, Y., et al. 2022, *ApJ*, 935, 31
 Humphreys, R. M., Helmel, G., Jones, T. J., & Gordon, M. S. 2020, *AJ*, 160, 145
 Itagaki, K. 2023, *TNSTR*, 2023-1158, 1
 Jacobson-Galan, W. V., Dessart, L., Margutti, R., et al. 2023, *ApJL*, 954, L42
 Jencson, J. E., Pearson, J., Beasar, E. R., et al. 2023, *ApJ*, 952, L30
 Kennicutt, R. C. J., & Garnett, D. R. 1996, *ApJ*, 456, 504
 Kewley, L. J., Geller, M. J., & Jansen, R. A. 2004, *AJ*, 127, 2002
 Kilpatrick, C. D., Foley, R. J., Jacobson-Galán, W. V., et al. 2023, *ApJL*, 952, L23
 Kobulnicky, H. A., Kennicutt, R. C. J., Pizagno, J. L., et al. 1999, *ApJ*, 514, 544
 Lin, L., Zou, H., Kong, X., et al. 2013, *ApJ*, 769, 127
 Lundquist, M., O’Meara, J., & Walawender, J. 2023, *TNSAN*, 160, 1
 Magg, E., Bergemann, M., Serenelli, A., et al. 2022, *A&A*, 661, A140
 Neustadt, J. M. M., Kochanek, C. S., & Rizzo Smith, M. 2023, *MNRAS*, Advance Access
 Niu, Z., Sun, N.-C., Maund, J. R., et al. 2023, *ApJL*, 955, L15
 Ofek, E. O., Sullivan, M., Shaviv, N. J., et al. 2014, *ApJ*, 789, 104
 Ou, P.-S., Chen, K.-J., Chu, Y.-H., & Tsai, S.-H. 2023, *ApJ*, 944, 34
 Perley, D. A., Gal-Yam, A., Irani, I., & Zimmerman, E. 2023, *TNSAN*, 119, 1
 Pledger, J. L., & Shara, M. M. 2023, *ApJL*, 953, L14
 Poznanski, D., Prochaska, J. X., & Bloom, J. S. 2012, *MNRAS*, 426, 1465
 Ramsey, L. W., Sebring, T. A., & Sneden, C. A. 1994, *Proc. SPIE*, 2199, 31
 Riess, A. G., Yuan, W., Macri, L. M., et al. 2022, *ApJL*, 934, L7
 Schlafly, E. F., & Finkbeiner, D. P. 2011, *ApJ*, 737, 103
 Schlegel, D. J., Finkbeiner, D. P., & Davis, M. 1998, *ApJ*, 500, 525
 Smith, N. 2014, *ARA&A*, 52, 487
 Smith, N., Pearson, J., Sand, D. J., et al. 2023, *ApJ*, 956, 46
 Soker, N. 2023, *RAA*, 23, 081002
 Soraisam, M. D., Szalai, T., Van Dyk, S. D., et al. 2023, *ApJ*, 957, 64
 Storey, P. J., & Hummer, D. G. 1995, *MNRAS*, 272, 41
 Tremonti, C. A., Heckman, T. M., Kauffmann, G., et al. 2004, *ApJ*, 613, 898
 Van Dyk, S. D., Srinivasan, S., Andrews, J. E., et al. 2023, arXiv:2308.14844
 York, D. G., Adelman, J., Anderson, J. E. J., et al. 2000, *AJ*, 120, 1579
 Zhang, R., & Yuan, H. 2023, *ApJS*, 264, 14